MDPI

Article

Translating Neutron Star Observations to Nuclear Symmetry Energy via Deep Neural Networks

Plamen G. Krastev

Research Computing, Faculty of Arts and Sciences, Harvard University, 52 Oxford Street, Cambridge, MA 02138, USA; plamenkrastev@fas.harvard.edu

Abstract: One of the most significant challenges involved in efforts to understand the equation of state of dense neutron-rich matter is the uncertain density dependence of the nuclear symmetry energy. In particular, the nuclear symmetry energy is still rather poorly constrained, especially at high densities. On the other hand, detailed knowledge of the equation of state is critical for our understanding of many important phenomena in the nuclear terrestrial laboratories and the cosmos. Because of its broad impact, pinning down the density dependence of the nuclear symmetry energy has been a long-standing goal of both nuclear physics and astrophysics. Recent observations of neutron stars, in both electromagnetic and gravitational-wave spectra, have already constrained significantly the nuclear symmetry energy at high densities. The next generation of telescopes and gravitational-wave observatories will provide an unprecedented wealth of detailed observations of neutron stars, which will improve further our knowledge of the density dependence of nuclear symmetry energy, and the underlying equation of state of dense neutron-rich matter. Training deep neural networks to learn a computationally efficient representation of the mapping between astrophysical observables of neutron stars, such as masses, radii, and tidal deformabilities, and the nuclear symmetry energy allows its density dependence to be determined reliably and accurately. In this work, we use a deep learning approach to determine the nuclear symmetry energy as a function of density directly from observational neutron star data. We show, for the first time, that artificial neural networks can precisely reconstruct the nuclear symmetry energy from a set of available neutron star observables, such as masses and radii as measured by, e.g., the NICER mission, or masses and tidal deformabilities as measured by the LIGO/VIRGO/KAGRA gravitational-wave detectors. These results demonstrate the potential of artificial neural networks to reconstruct the symmetry energy and the equation of state directly from neutron star observational data, and emphasize the importance of the deep learning approach in the era of multi-messenger astrophysics.

Keywords: neutron stars; gravitational waves; equation of state; dense matter; nuclear symmetry energy

1. Introduction

Understanding the equation of state (EOS) of dense neutron-rich matter in terms of the fundamental interactions between its constituents is an extraordinarily challenging problem and represents a key outstanding question in modern physics and astrophysics [1–3]. Due to its broad ramifications for many important phenomena, ranging from understanding the heavy ion collision dynamics in nuclear laboratories to the most violent cosmic events, such as binary neutron star (BNS) mergers and supernovae, to gravitational waves, the determination of the EOS of dense matter has been a major shared goal of both the nuclear physics (see, e.g., Refs. [4–13]) and astrophysics (see, e.g., Refs. [14–35]) communities. It has been a primary scientific thrust for establishing key research facilities in astrophysics [1] and nuclear physics [2], such as large ground-based telescopes, advanced X-ray space-borne observatories, the Neutron Star Interior Composition Explorer (NICER) [36], LIGO/VIRGO/KAGRA [37–39] gravitational-wave detectors, and all advanced radioactive beam laboratories around the globe.

In cold neutron star matter, the nucleonic component of the EOS can be written in terms of the energy per nucleon ρ as [40]

$$E(\rho, \delta) = E_{SNM}(\rho) + E_{sym}(\rho)\delta^2, \tag{1}$$

where $E_{SNM}(\rho) = E(\rho, 0)$ is the energy per nucleon of symmetric nuclear matter (SNM), $E_{sym}(\rho)$ is the symmetry energy, and $\delta = (\rho_n - \rho_p)/\rho$ is the isospin asymmetry, with ρ_n, ρ_p, and $\rho = \rho_n + \rho_p$ being the neutron, proton, and total density, respectively. Presently, the EOS of cold nuclear matter under extreme conditions of density, pressure, and/or isospin asymmetry still remains rather uncertain and theoretically controversial, particularly at supra-saturation densities, mainly due to the poorly known high-density behavior of the nuclear symmetry energy $E_{sym}(\rho)$ [4,5].

To determine the EOS from first principles, we need to solve quantum chromodynamics (QCD), which is the fundamental theory of strong interactions. However, at present, model-independent results are only available for a rather limited density range. At low densities of $\rho \sim [1-2]\rho_0{}^1$, we can use *ab initio* approaches together with nuclear interaction derived from Chiral Effective Theory (χEFT) with controlled uncertainty estimates [41–50]. At asymptotically high densities of $\rho \gtrsim 50\,\rho_0$, perturbative QCD calculations converge and provide reliable results [51–57]. At intermediate densities of $\rho \sim [2-10]\rho_0$, however, there are still no reliable QCD predictions [58]. To derive the EOS from QCD in the intermediate-density region, one needs to develop non-perturbative approaches, such as the Monte Carlo simulation of QCD on a lattice (lattice QCD), but the application of these methods to systems at finite densities is hindered by the notorious sign problem; see, e.g., Ref. [59]. Therefore, at intermediate densities, the EOS construction still relies on phenomenological approaches employing a variety of many-body methods and effective interactions, such as the relativistic mean field theory, and density functionals based on the Skyrme, Gogny, or Similarity Renormalization Group (SRG) evolved interactions.

Meanwhile, we have witnessed extraordinary progress in efforts to constrain the high-density EOS from both nuclear laboratory experiments with radioactive beams, and multi-messenger astrophysical (MMA) observations of neutron stars. In particular, extensive analyses of experimental data of heavy-ion reactions from intermediate to relativistic energies, especially various forms of nucleon collective flow and the kaon production, have already constrained significantly the EOS of SNM up to approximately 4.5 ρ_0; see, e.g., Ref. [6]. In addition, thanks to the great efforts and collaboration of both the nuclear physics and astrophysics communities, significant progress has been made in the last two decades in constraining the symmetry energy around, and below, nuclear matter saturation density using results from both astrophysical observations and terrestrial nuclear experiments; see, e.g., Refs. [5,9–11,60–63]. However, the poorly known density dependence of the nuclear symmetry energy $E_{sym}(\rho)$ at supra-saturation densities, and the possible hadron-to-quark phase transition, still remain the most uncertain aspects of the EOS of dense matter [4,5,21,22,24]. Furthermore, the appearance of various new particles, such as hyperons and resonances, is also strongly dependent upon the high-density trend of $E_{sym}(\rho)$ [64–79]. Because, above the hadron-to-quark transition density, the nuclear symmetry energy would naturally lose its physical meaning, it is critical to determine simultaneously both the high-density behavior of the symmetry energy and the detailed properties of the hadron-to-quark phase transition, analyzing combined data from astrophysical observations and nuclear laboratory experiments [5].

Recent MMA observations of neutron stars provide unique means to probe the high-density EOS and, in particular, the $E_{sym}(\rho)$ at densities currently inaccessible in the nuclear laboratories. Moreover, these new advances in neutron star (NS) observations have opened an alternative pathway for the model-independent extraction of the symmetry energy, and the EOS, via statistical approaches (see, e.g., Refs. [35,80–85]). These observations include the Shapiro delay measurements of massive $\sim 2M_\odot$ pulsars [86–88], the radius measurement of quiescent low-mass X-ray binaries and thermonuclear bursters [80–82,89,90], the X-ray timing measurements of pulsars by the NICER mission [91,92], and the detection

and inference of gravitational waves from compact binary mergers involving NSs by the LIGO/VIRGO/KAGRA collaboration [93–95]. Typical NS observables include mass M, radius R, moment of inertia I, quadrupole moment Q, dimensionless tidal deformability Λ (and derivatives, e.g., Love number k_2 and tidal deformability λ), and compactness M/R. Specifically, the NICER mission aims at the compactness M/R of NSs by measuring the gravitational lensing of the thermal emission from the stellar surface. On the other hand, gravitational-wave (GW) observations of BNS and neutron star–black hole (NSBH) mergers provide information on the tidal disruption of the star in the presence of its companion, quantified by the tidal deformability parameter λ. Some of these NS observables are related via EOS-independent universal relations, such as the well-known I-Love-Q relation, which relates I, k_2, and Q [96,97].

There is a plethora of diverse statistical approaches to construct the most probable EOS from NS observational data, with the Bayesian inference [35,80–84] as the most commonly used technique at the present. There are also other methods, such as those based on the Gaussian processes, which are variants of the Bayesian inferences with nonparametric representation of the EOS; see, e.g., Ref. [85]. Despite the significant effort to extract the genuine EOS from the NS astrophysical data, it is still unclear what the *true* dense matter EOS should look like, mainly due to the uncertainties of the assumed prior distributions in the Bayesian analyses [58]. Therefore, the need arises for alternative approaches to construct the model-independent EOS. Recently, approaches based on deep neural networks (DNNs) have gained interest in the research community and have been extensively explored and applied in a wide range of scientific and technical domains. Deep learning (DL) algorithms, a subset of machine learning (ML), are highly scalable computational techniques with the ability to learn directly from raw data, employing artificial neurons arranged in stacked layers, named neural networks, and optimization methods based on gradient descent and back-propagation [98,99]. These techniques, especially with the aid of GPU computing, have proven to be highly successful in tasks such as image recognition [100], natural language processing [101], and recently also emerged as a new tool in engineering and scientific applications, alongside traditional High-Performance Computing (HPC) in the new field of Scientific Machine Learning [102]. DL approaches have been already successfully applied in a wide range of physics and astrophysics domains; see, e.g., Refs. [103–113]. In particular, DL has been applied in GW data analysis for the detection [114–121], parameter estimation [122,123], and denoising [124] of GW signals from compact binary mergers. In previous works [125,126], we also pioneered the use of DL methods, specifically Convolutional Neural Network (CNN) [127] algorithms, for the detection and inference of GW signals from BNS mergers embedded in both Gaussian and realistic LIGO noise. Several studies have also explored the DL approach as a tool to extract the dense matter EOS from NS observations [58,128–131].

In this work, we explore a DL approach to extract the nuclear symmetry energy $E_{sym}(\rho)$, the most uncertain part of the EOS, directly from NS astrophysical data. Specifically, we train DNNs to map pairs of NS mass and radius $M - R$, or stellar mass and tidal deformability $M - \Lambda$, to $E_{sym}(\rho)$. We show, for the first time, that DL can be used to infer the nuclear symmetry energy directly from NS observational data accurately and reliably. Most importantly, we show that DL algorithms can be used successfully to construct a model-independent $E_{sym}(\rho)$ and therefore determine precisely the density dependence of the nuclear symmetry energy at supra-saturation densities. These results are a step towards achieving the goal of determining the EOS of dense neutron-rich matter, and emphasize the potential and importance of this DL approach in the MMA era, as an ever-increasing volume of NS observational data becomes available with the advent of the next generation of large telescopes and GW observatories.

This paper is organized as follows. After the introductory remarks in this section, in Section 2, we discuss the main features and parameterization of the EOS applied in this work. In Section 3, we briefly recall the formalism for solving the structure equations of static NSs and calculating the tidal deformability. In Section 4, we discuss the DL approach

used to map the NS observables to the nuclear symmetry energy. We present our results in Section 5. At the end, we conclude in Section 6 with a short summary and outlook on future investigations.

Conventions: We use units in which $G = c = 1$.

2. Equation of State

The EOS is the major ingredient for solving the NS structure equations and calculating global stellar properties, such as mass M, radius R, and dimensionless tidal deformability Λ. The most commonly used theoretical approaches to determine the nuclear EOS fall into two major categories—phenomenological and microscopic methods. Phenomenological approaches are based on effective interactions constructed to describe the ground state of finite nuclei and therefore applications to systems at high isospin asymmetries must be considered with care [132]. Moreover, at large densities, no experimental data are available to constrain such interactions and therefore predictions based on these methods could be very different from the realistic behavior. Among the most used phenomenological approaches are methods based on Skyrme interactions [133,134] and relativistic mean-field (RMF) models [135]. On the other hand, microscopic approaches start with realistic two-body and three-body nucleon forces that describe accurately free-space nucleon scattering data and the deuteron properties. Such interactions are either based on meson-exchange theory [136,137], or recent χEFT [46,138–140]. The major challenge for the many-body methods is the treatment of the short-range repulsive core of the nucleon–nucleon interaction, and this represents the difference among the available techniques. Among the most well-known microscopic many-body methods are the Brueckner–Hartree–Fock (BHF) approach [141] and its relativistic counterpart, the Dirac–Brueckner–Hartree–Fock (DBHF) theory [142,143], the variational approach [144], the Quantum Monte Carlo technique and its derivatives [145,146], the self-consistent Green's function technique [147], the χEFT [49], and the $V_{low\,k}$ approach [148].

Around saturation density ρ_0, the $E_{SNM}(\rho)$ and $E_{sym}(\rho)$ predicted by many-body theories can be Taylor expanded as

$$E_{SNM}(\rho) = E_0 + \frac{K_0}{2}x^2 + \frac{J_0}{6}x^3, \tag{2}$$

$$E_{sym}(\rho) = S_0 + Lx + \frac{K_{sym}}{2}x^2 + \frac{J_{sym}}{6}x^3, \tag{3}$$

with $x \equiv (\rho - \rho_0)/3\rho_0$. The expansion coefficients in these expressions can be constrained by nuclear experiments and have the following meanings [149]: $E_0 \equiv E_{SNM}(\rho_0)$, $K_0 \equiv [9\rho^2 d^2 E_{SNM}/d\rho^2]_{\rho_0}$, and $J_0 \equiv [27\rho^3 d^3 E_{SNM}/d\rho^3]_{\rho_0}$ are the binding energy, incompressibility, and skewness of SNM; $S_0 \equiv E_{sym}(\rho_0)$, $L \equiv [3\rho dE_{sym}/d\rho]_{\rho_0}$, $K_{sym} \equiv [9\rho^2 d^2 E_{sym}/d\rho^2]_{\rho_0}$, and $J_{sym} \equiv [27\rho^3 d^3 E_{sym}/d\rho^3]_{\rho_0}$ are the magnitude, slope, curvature, and skewness of the symmetry energy at ρ_0. Currently, the most probable values of these parameters are as follows: $E_0 = -15.9 \pm 0.4$ MeV, $K_0 = 240 \pm 20$ MeV, $-300 \leq J_0 \leq 400$ MeV, $S_0 = 31.7 \pm 3.2$ MeV, $L = 58.7 \pm 28.1$ MeV, $-400 \leq K_{sym} \leq 100$ MeV, and $-200 \leq J_{sym} \leq 800$ MeV; see e.g., Ref. [150]. Although, at higher densities, the Taylor expansions diverge themselves [151], Equations (2) and (3) can also be viewed as parameterizations where, in principle, the parameters are left free [150]. In this respect, the above relations have dual meanings. Namely, for systems with low isospin asymmetries, they are Taylor expansions near the saturation density, while, for very neutron-rich systems at supra-saturation densities, they should be regarded as parameterizations [150]. For further discussion on the relationship between the *Taylor expansions* and the parameterizations adopted in our analysis, the reader is referred to, e.g., Ref. [150]. These parameterizations are often used in *metamodeling* of the NS EOS and have been applied previously, for instance, in solving the NS inverse-structure problem and constraining the high-density symmetry energy by astrophysical observations of NSs [150,152]. The NS EOS metamodel has been also applied in Bayesian analyses to extract the most probable values of the high-density parameters

of the EOS, where the posterior Probability Distribution Functions (PDFs) of the EOS parameters and their correlations are inferred directly from NS observational data [153]. The parameterizations described here have the advantage, over the widely used piecewise polytropes for directly parameterizing the pressure as a function of energy or baryon density of NS matter, of keeping the isospin dependence of the EOS, and they explicitly retain information on the composition for the whole density range, without losing the ability to model a wide range of EOSs as predicted by various many-body approaches. This feature of the metamodeling approach is particularly important for inferring the high-density symmetry energy parameters, or directly $E_{sym}(\rho)$, as it clearly separates the contribution of $E_{sym}(\rho)$ to the EOS.

For the purpose of our analysis, in the present study, we adopt the EOS metamodel described briefly above and, by varying the EOS parameters, generate a large number of EOSs and corresponding $M - R$, or $M - \Lambda$ sequences, by solving the NS structure equations. We assume a simple model of matter in the NS core consisting of protons, neutrons, electrons, and muons (the $npe\mu$-model) in β-equilibrium. With $E_{SNM}(\rho)$ and $E_{sym}(\rho)$, parameterized by Equations (2) and (3), $E(\rho, \delta)$ is calculated through Equation (1). Then, the pressure of NS matter in β-equilibrium

$$P(\rho, \delta) = \rho^2 \frac{d\epsilon(\rho, \delta)/\rho}{d\rho} \tag{4}$$

can be computed from the energy density $\varepsilon(\rho, \delta) = \rho[E_n(\rho, \delta) + M_N] + \varepsilon_l(\rho, \delta)$, where M_N is the average nucleon mass and $\varepsilon_l(\rho, \delta)$ is the lepton energy density. Details for calculating $\varepsilon_l(\rho, \delta)$ can be found in, e.g., Ref. [154]. Below approximately 0.07 fm^{-3}, the core EOS is supplemented by a crustal EOS, which is more suitable at lower densities. For the inner crust, we apply the EOS by Pethick et al. [155] and, for the outer crust, the one by Haensel and Pichon [156].
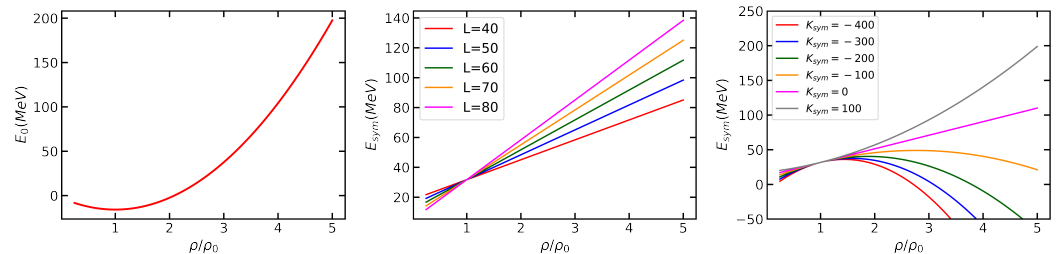
Figure 1. (**Left window**) Energy per particle of SNM as a function of the reduced density ρ/ρ_0. The EOS of SNM is kept fixed by setting all parameters in Equation (1). Specifically, we set $E_0 = 15.9$ MeV, $K_0 = 240$ MeV, and $J_0 = 0$ MeV. (**Middle window**) Symmetry energy E_{sym} as a function of ρ/ρ_0 for $L = 40, 50, 60, 70, 80$ MeV, with $K_{sym} = 0$ MeV. (**Right window**) Same as the middle window but for $K_{sym} = -400, -300, -200, -100, 0, 100$ MeV, with $L = 58.7$ MeV. In both middle and right windows, $S_0 = 31.7$ MeV and $J_{sym} = 0$ MeV. See text for details.

We use Equations (2) and (3) as parameterizations, together with the parabolic approximation of the nucleonic EOS Equation (1), and fix E_0, K_0, and S_0 at their most probable currently known values from nuclear laboratory experiments and/or nuclear theories. Since the main focus of this analysis is specifically on extracting $E_{sym}(\rho)$ from NS observables, we fix the SNM EOS, $E_{SNM}(\rho)$, by setting $J_0 = 0$ MeV, and vary only $E_{sym}(\rho)$. The J_0 parameter controls the stiffness of the SNM EOS and in turn the maximum NS mass M_{max} of the resultant stellar models. The maximum NS mass of 2.14 $M_\odot$ observed so far [88] requires J_0 to be larger than -200 MeV, depending slightly on the symmetry energy parameters [157]. At present, the predicted range of J_0 still has relatively large uncertainties [157], which also partially justifies our choice of setting $J_0 = 0$. With $E_{SNM}(\rho)$ kept fixed, the EOS is therefore solely determined by $E_{sym}(\rho)$. The EOS of SNM $E_{SNM}(\rho)$ is shown in the left window of Figure 1. For the purpose of our analysis, we also set the symmetry energy skewness parameter $J_{sym} = 0$ MeV. This choice is also partially justified

by the very large uncertainty range of J_{sym} at present [157], but the main reason for setting $J_{sym} = 0$ is to simplify our problem. In following works, we plan to consider the effect of both J_0 and J_{sym}. This would allow for the modeling of a wider class of EOSs as predicted by various many-body approaches, and models of the nuclear interaction. Together with using realistic NS astrophysical observations, this data-driven approach would allow for extracting realistic symmetry energies, and in turn the EOS. With the above choices, we subsequently vary the symmetry energy parameters L and K_{sym} to generate many samples of $E_{sym}(\rho)$, and the EOS. The effect of varying the L and K_{sym} parameters on the symmetry energy is illustrated in the middle and right windows of Figure 1. While, in principle, these parameters are absolutely free, the asymptotic boundary conditions of the EOS near ρ_0 and $\delta = 0$ provide some prior knowledge of the ranges of these parameters. The ranges of L and K_{sym} are further restricted by imposing the requirement that the EOSs satisfy causality, and the resultant NS models can support a maximal mass of at least 2.14 $M_\odot$. The ranges of the symmetry energy $E_{sym}(\rho)$ and pressure P satisfying all constraints are shown in Figure 2.
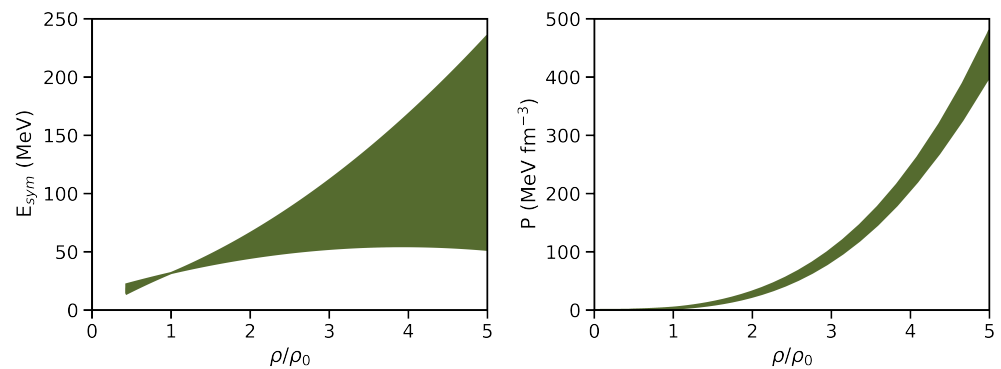
Figure 2. Range of the nuclear symmetry energy E_{sym} (**left window**) and pressure P (**right window**). The E_{sym} and P are plotted as functions of the reduced density ρ/ρ_0.

3. Neutron Star Structure Equations and Tidal Deformability

In this section, we briefly review the formalism for calculating the NS mass M, radius R, and tidal deformability λ. For a spherically symmetric relativistic star, the Einstein's field equations reduce to the familiar Tolaman–Oppenheimer–Volkoff (TOV) [158] equation:

$$\frac{dp(r)}{dr} = -\frac{\varepsilon(r)m(r)}{r^2}\left[1 + \frac{p(r)}{\varepsilon(r)}\right]\left[1 + \frac{4\pi r^3 p(r)}{m(r)}\right]\left[1 - \frac{2m(r)}{r}\right]^{-1}, \tag{5}$$

where the gravitational mass within a sphere of radius r is determined by

$$\frac{dm(r)}{dr} = 4\pi\varepsilon(r)r^2. \tag{6}$$

To proceed with the solution of the above equations, one needs to provide the EOS of stellar matter in the form $p(\varepsilon)$. Starting from some central energy density $\varepsilon_c = \varepsilon(r = 0)$ at the center of the star, with the initial condition $m(0) = 0$, Equations (5) and (6) can be integrated until p vanishes, signifying that the edge of the star has been reached. Some care should be taken at $r = 0$ since, as seen above, the TOV equation is singular there. The point $r = R$ where p_0 vanishes defines the NS radius and $M = m(R) = 4\pi \int_0^R \varepsilon(r')r'^2 dr'$ determines the NS gravitational mass.

For a given EOS, there is a unique relationship between the stellar mass and the central density ε_c. Thus, for a particular EOS, there is a unique sequence of NSs parameterized by the central density (or equivalently the central pressure $p_c = p(0)$). The range of the $M - R$ relation computed with the EOSs considered in this work is shown in the left window of Figure 3.

The tidal deformability λ is a parameter quantifying the tidal deformation effects experienced by NSs in coalescing binary systems during the early stages of an inspiral. This parameter is defined as [159–161]

$$\lambda = -\frac{Q_{ij}}{\mathcal{E}_{ij}}, \tag{7}$$

where Q_{ij} is the induced mass quadruple moment of an NS in the gravitational tidal field $\mathcal{E}_{ij}$ of its companion. The tidal deformability can be expressed in terms of the NS radius, R, and dimensionless tidal Love number, k_2, as

$$\lambda = \frac{2}{3}k_2 R^5. \tag{8}$$

The tidal Love number k_2 is calculated using the following expression [162,163]:

$$
\begin{aligned}
k_2(\beta, y_R) & = \frac{8}{5}\beta^5(1 - 2\beta)^2[2 - y_R + 2\beta(y_R - 1)] \\
& \times \{2\beta[6 - 3y_R + 3\beta(5y_R - 8)] \\
& + 4\beta^3[13 - 11y_R + \beta(3y_R - 2) \\
& + 2\beta^2(1 + y_R)] + 3(1 - 2\beta)^2[2 - y_R \\
& + 2\beta(y_R - 1)]\ln(1 - 2\beta)\}^{-1},
\end{aligned}
\tag{9}
$$

where $\beta \equiv M/R$ is the dimensionless compactness parameter and $y_R \equiv y(R)$ is the solution of the following first-order differential equation (ODE):

$$\frac{dy(r)}{dr} = -\frac{y(r)^2}{r} - \frac{y(r)}{r}F(r) - rQ(r), \tag{10}$$

with

$$F(r) = \left\{1 - 4\pi r^2[\varepsilon(r) - p(r)]\right\}\left[1 - \frac{2m(r)}{r}\right]^{-1}, \tag{11}$$

$$
\begin{aligned}
Q(r) & = 4\pi\left[5\varepsilon(r) + 9p(r) + \frac{\varepsilon(r) + p(r)}{c_s^2(r)} - \frac{6}{r^2}\right]\left[1 - \frac{2m(r)}{r}\right]^{-1} \\
& - \frac{4m^2(r)}{r^4}\left[1 + \frac{4\pi r^3 p(r)}{m(r)}\right]^2\left[1 - \frac{2m(r)}{r}\right]^{-2},
\end{aligned}
\tag{12}
$$

where $c_s^2(r) \equiv dp(r)/d\varepsilon(r)$ is the squared speed of sound. Starting at the center of the star, for a given EOS, Equation (10) needs to be integrated self-consistently together with Equations (5) and (6). Imposing the additional boundary condition for y at $r = 0$ such that, $y(0) = 2$, the Love number k_2 and the tidal deformability λ can be readily calculated. One can also compute the dimensionless tidal deformability Λ, which is related to the compactness parameter β and the Love number k_2 through

$$\Lambda = \frac{2}{3}\frac{k_2}{\beta^5}. \tag{13}$$

The range of Λ as a function of the stellar mass is shown in the right window of Figure 3.
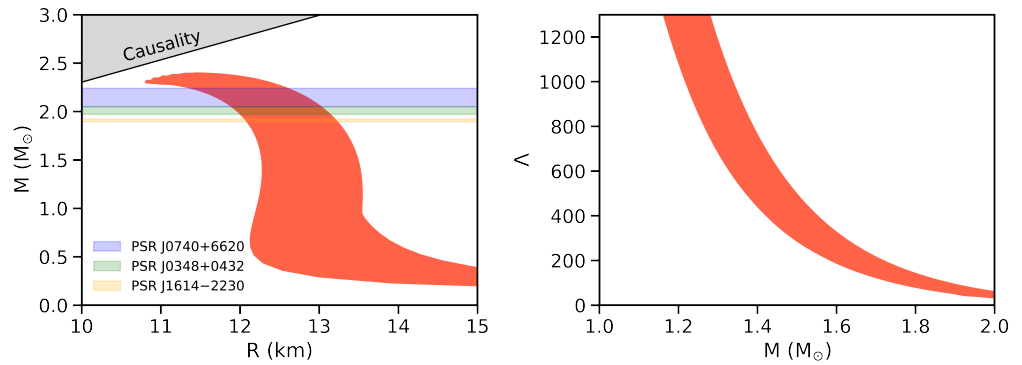
Figure 3. Range of mass–radius relation (**left window**) and dimensionless tidal deformability Λ (**right window**) for the EOSs considered in this study. Λ is plotted as a function of stellar mass *M*. The mass ranges of the three heaviest pulsars known at present [86–88] are indicated in the left window.

The total tidal effect of two neutron stars in an inspiraling binary system is given by the mass-weighted (dimensionless) tidal deformability (see, e.g., Refs. [159,161]):

$$\tilde{\Lambda} = \frac{16}{13} \frac{(M_1 + 12M_2)M_1^4 \Lambda_1 + (M_2 + 12M_1)M_2^4 \Lambda_2}{(M_1 + M_2)^5}, \tag{14}$$

where $\Lambda_1 = \Lambda_1(M_1)$ and $\Lambda_2 = \Lambda_2(M_2)$ are the (dimensionless) tidal deformabilities of the individual binary components. As pointed out previously [159], although Λ is calculated for single neutron stars, the universality of the neutron star EOS allows us to predict the tidal phase contribution for a given binary system from each EOS. For equal-mass binary systems, $\tilde{\Lambda}$ reduces to Λ. The weighted (dimensionless) deformability $\tilde{\Lambda}$ is usually plotted as a function of the chirp mass $\mathcal{M} = (M_1 M_2)^{3/5}/M_T^{1/5}$ for various values of the asymmetric mass ratio $\eta = M_1 M_2 / M_T^2$, where $M_T = M_1 + M_2$ is the total mass of the binary.

4. Deep Neural Networks (DNNs)

In this section, we briefly discuss the basic setup, structure, and workflow associated with implementing DNNs for our specific application. For more extensive discussions, the reader is referred to a number of machine learning articles [98,164] and textbooks [99,165].

Deep neural networks consist of processing units, named neurons, which are arranged in one to several layers (Figure 4a). A neuron acts as a filter, performing a linear operation between the neurons in the previous layer and the weights associated with the neuron. A DNN typically has an input layer, followed by one or more hidden layers, and a final layer with one or more output neurons. As illustrated in Figure 4a, in a *feedforward* DNN, calculations progress (from left to right) starting at the input layer and moving successively through the hidden layers until reaching the output layer. In classification problems, the output neurons give the probabilities that an input sample belongs to a specific class. In regression problems, the output layer returns estimates of one or several target parameters. Each neuron in a DNN performs a simple linear operation. Namely, for input values x_i from the previous layer, it outputs a single value $a = f(\sum x_i w_i + b)$; see Figure 4b,c. *Activation* functions f depend on the specific application but are typically chosen to be nonlinear or piecewise functions, such as the sigmoid or hyperbolic tangent functions [166] (Figure 4b). The weights w_i and bias b are unique to each neuron and are parameters that are tuned iteratively via a backpropagation algorithm during the DNN training (Figure 4b). Neuron k in layer m accepts the outputs $a_1^{m-1}, a_2^{m-1}, \ldots, a_N^{m-1}$ from all N from the previous layer $m-1$ and computes a single value $a_k^m = f(\sum a_i^{m-1} w_i + b)$ that is broadcasted to every neuron in layer $m+1$ [165].
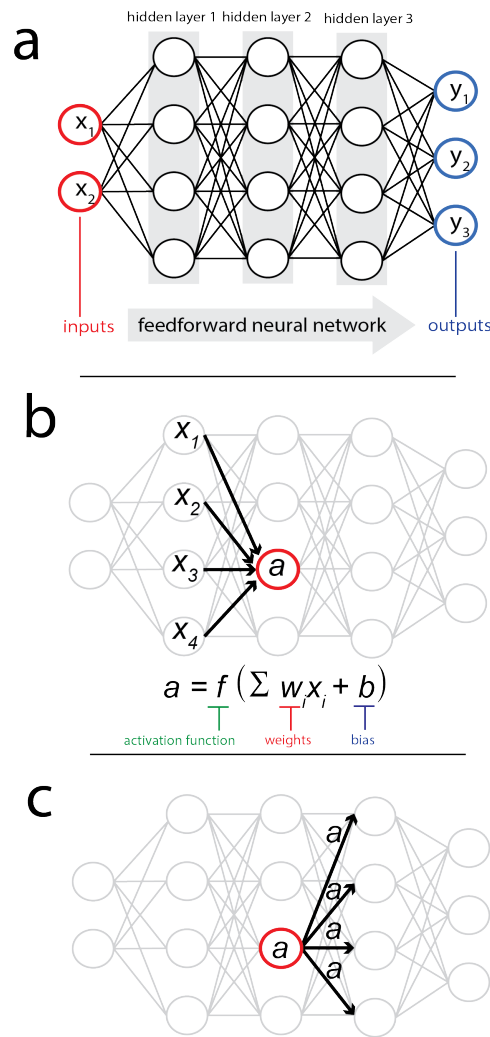
Figure 4. (**a**) Structure of an example deep neural network with input, hidden, and output layers highlighted. In the feedforward neural networks used in this study, calculations move from left to right, as illustrated in the figure. (**b**) Inputs to an example neuron from the previous layer. Also shown is the calculation performed by the example neuron, with inputs weighted relative to one another, bias added, and an activation function applied, in order to calculate a value *a*, referred to as the activation of the neuron. (**c**) The activation of the example neuron serves as one of the inputs to the next layer of neurons. Each neuron in the successive layers of the DNN is performing this same operation with different values of the tunable parameters w_i and b, within the backpropagation algorithm. See text for details.

In this analysis, we apply a DL approach and formulate a regression problem, where the inputs to the DNNs consist of $M(R)$ or $M(\Lambda)$ sequences, while the outputs consist of $E_{sym}(\rho)$ estimates. Accordingly, the data sets consist of $E_{sym}(\rho)$ samples and $M(R)$, or $M(\Lambda)$, sequences. We use the EOS metamodel discussed in Section 2, with the SNM part of the EOS kept fixed, and vary only the symmetry energy. In particular, we set $E_0 = 15.9$ MeV, $K_0 = 240$ MeV, $J_0 = 0$ MeV, $S_0 = 31.7$ MeV, $J_{sym} = 0$, and vary only L and K_{sym} in Equations (2) and (3). Specifically, the values of L and K_{sym} are sampled randomly from their respective ranges of [30.6–86.8] MeV and [−400–100] MeV. Recently, the latest results of the PREX collaboration suggested a rather high value of L with an upper limit at 143 MeV [167]. Examining the effect of higher L values is left to following works. The resultant EOSs $p(\varepsilon)$ are checked regarding whether they satisfy (i) the microscopic stability condition, i.e., $\frac{dp}{d\varepsilon} \geq 0$, and (ii) the causality condition, i.e., the speed of sound $c_s \equiv \sqrt{\frac{dp}{d\varepsilon}} \geq c$, which restricts the values of L and K_{sym} and the $E_{sym}(\rho)$ samples. For

each EOS, the NS structure equations are solved to obtain $M(R)$ and $M(\Lambda)$ sequences. To simulate NS observational data, from a given genuine $M - R$ (or $M - \Lambda$) sequence, we randomly choose 50 points in the range of $1M_\odot$ to $2M_\odot{}^2$. Then, each sample input is a vector of dimension 100, with the two arrays of M and R (or M and Λ) values concatenated. Similarly, each output sample is a vector of dimension 100 representing an estimated $E_{sym}(\rho)$ in the density range of $\sim 0.5\rho/\rho_0$ to $5\rho/\rho_0$. In this respect, the DNN maps an input $M(R)$ or $M(\Lambda)$ sequence to an output $E_{sym}(\rho)$. Realistic NS observations inevitably accrue errors, which result in corresponding uncertainties when reconstructing the symmetry energy, and/or the EOS. For the purpose of this analysis, however, we do not take into account NS observational errors and uncertainties. This work should be regarded as a *proof-of-concept study*, and the application to realistic NS data is left to a future article.

In supervised learning, the data sets are divided into training, validation, and testing data. The training data set is used by the DNN to learn from, the validation data are used to verify whether the network is learning correctly, and the testing data are used to assess the performance of the trained model. The training data sets used in this work consist of 40,000 independent $M(R)$, or $M(\Lambda)$, sequences representing the DNN inputs, and 40,000 matching $E_{sym}(\rho)$ samples representing the DNN outputs. The validation and testing data sets consist of ~ 1000 input samples and the same number of output samples each.

The neural networks used here are feedforward DNNs with 10 hidden, dense, fully connected layers of dimension 100, and *ReLU* activation functions. The first layer has a linear activation function and corresponds to the input to the neural network, which, in this case, is a one-dimensional concatenated vector containing the NS M and R (or Λ) values for a given $M(R)$ (or $M(\Lambda)$) sequence. At the end, there is a linear output layer of dimension 100 returning the estimated $E_{sym}(\rho)$. The network design was optimized by fine-tuning multiple hyper-parameters, which include here the number and type of network layers, the number of neurons in each layer, and the type of activation function. The optimal network architecture was determined through multiple experiments and tuning of the hyper-parameters. The feedforward DNN used in this work and its functionality is shown schematically in Figure 4.

To build and train the neural networks, we used the Python toolkit Keras (https://keras.io (accessed on 28 September 2021)), which provides a high-level application programming interface (API) to the TensorFlow [168] (https://www.tensorflow.org (accessed on 28 September 2021)) deep learning library. We applied the technique of stochastic gradient descent with an adaptive learning rate with the ADAM method [169] with the AMSgrad modification [170]. To train the DNNs, we used an initial learning rate of 0.003 and chose a batch size of 500. During each training session, the number of epochs was limited to 2000, or until the validation error stopped decreasing. The training of the DNNs was performed on an NVIDIA Tesla V100 GPU and the size of the mini-batches was chosen automatically depending on the specifics of the GPU and data sets. We used the mean squared error (MSE) as a cost (or loss) function.

5. Results

We first examine the ability of the DNN to reconstruct the $E_{sym}(\rho)$ from a set of mass and radius $M - R$ measurements that may result from electromagnetic observations of neutron stars, such as those from the NICER mission, for instance. Specifically, we apply the trained DNN, described in the previous section, to a test data set containing ~ 1000 simulated $M(R)$ sequences, and compare the corresponding estimated output $E_{sym}(\rho)$ with the exact symmetry energy for each sample. In Figure 5, we show results for five representative examples from the test data set. It is seen that the estimated symmetry energy (broken colored lines) for each input $M - R$ sequence matches almost exactly the "true" $E_{sym}(\rho)$ (solid black lines) over the entire density range considered here. The results are very similar for the rest of the test data samples. Quantitatively, at $5\rho_0$, the mean absolute error over the whole test data set is 1.2 MeV, with a standard deviation of 0.8 MeV, where the errors are even smaller at lower densities. Choosing different ensembles of randomly

selected points from the genuine $M(R)$ curves does not alter appreciably the accuracy with which the symmetry energy is estimated.
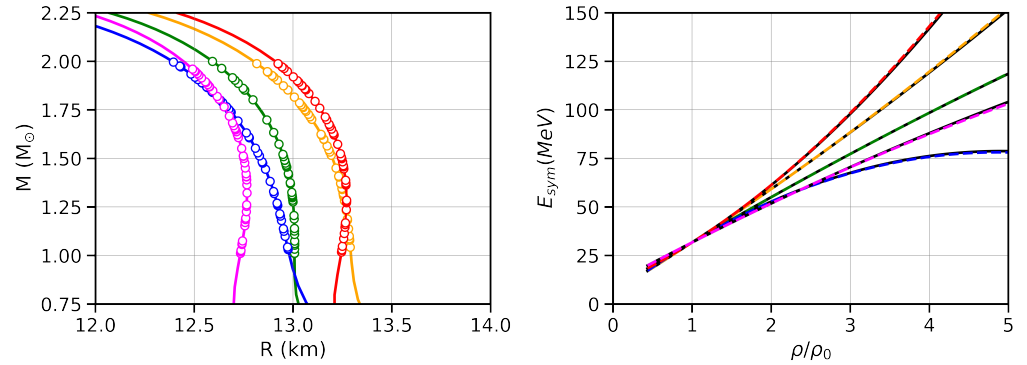
Figure 5. Example input $M(R)$ sequences (**left window**) and corresponding estimated $E_{sym}(\rho)$ (**right window**). The input samples consist of 50 randomly selected points, denoted by the "o" characters, from the genuine $M(R)$ curves, denoted by the solid lines, in the range of 1–2 $M_{\odot}$. The output data samples consist of 100 $E_{sym}(\rho)$ points in the range of $\sim$0.4–5 ρ_0. Broken colored lines in the right window denote the estimated $E_{sym}(\rho)$ and the solid lines represent the exact $E_{sym}(\rho)$. Same curve colors in both windows denote pairs of input $M(R)$ sequences and corresponding output symmetry energy.

At this point, we need to reiterate that realistic NS observations inevitably carry uncertainties, which would result in corresponding uncertainties in the estimated symmetry energy. However, this work should be considered a "proof-of-concept study" and realistic applications are left for following articles. In addition, these results are based on the assumption that we have 50 NS $M - R$ observations. Although, at present, such a large number may seem rather optimistic, with the advent of the next generation of electromagnetic observatories, this circumstance is rapidly changing as many more NS electromagnetic observations are expected in the future. These results clearly demonstrate the ability of the DL-based approach to extract the nuclear symmetry energy accurately from NS mass and radius measurements, given that observational data of sufficient quality exist.

We next look at the ability of the neural network to extract the symmetry energy entirely from GW data from compact binary mergers involving neutron stars, particularly BNS events. Specifically, we assume a set of mass and tidal deformability $M - \Lambda$ measurements that may result from the LIGO/VIRGO/KAGRA GW detectors, and from the next-generation GW ground-based (e.g., Einstein Telescope and the Cosmic Explorer) and space-borne (e.g., LISA) observatories, in the future. In this case, the trained DNN model is applied to a test data set containing $\sim$1000 simulated $M(\Lambda)$ sequences, and the estimated output $E_{sym}(\rho)$ is compared with the exact symmetry energy for each data sample. The results are summarized in Figure 6, which shows five representative examples from the test data set. Again, the estimated $E_{sym}(\rho)$ (broken colored lines) follows very closely the "true" symmetry energy (solid black lines) for each input $M - \Lambda$ sequence over the entire density range, and the results follow a very similar trend for all samples in the test data set. The overall performance of the DNN is again assessed by looking at the mean absolute error, which, at 5ρ_0, is 0.8 MeV, with a standard deviation of 0.4 MeV. As discussed in the previous section, the input of the neural network consists of 50 randomly chosen points from a given genuine $M(\Lambda)$ curve in the range of 1–2 $M_{\odot}$, and the output consists of 100 fixed points of $E_{sym}(\rho)$ in the range $\sim$0.4–5 ρ_0. Using different input ensembles of randomly selected points does not change significantly the results presented in Figure 6. These findings show that the $E_{sym}(\rho)$ can be extracted accurately, via artificial neural networks, directly from GW observational data of neutron stars. They also emphasize the importance of the DL-based approach for extracting the symmetry energy, the most uncertain component of the dense matter EOS, from GW observations. As in the case of NS mass and radius measurements, GW observations of neutron stars inevitably accrue errors, which result in

corresponding uncertainties in the extracted symmetry energy, and the EOS. As already mentioned, realistic applications of the DL method are left to following works.

These novel computational techniques will become particularly important in the future with the advent of the next generation GW observatories, when millions of GW events will be routinely detected per year, with at least several events involving neutron stars per day. As more such GW events are detected and characterized, this data-driven approach will eventually allow us to map precisely the GW observations of neutron stars to the $E_{sym}(\rho)$, and in turn, the underlying EOS of dense nuclear matter.
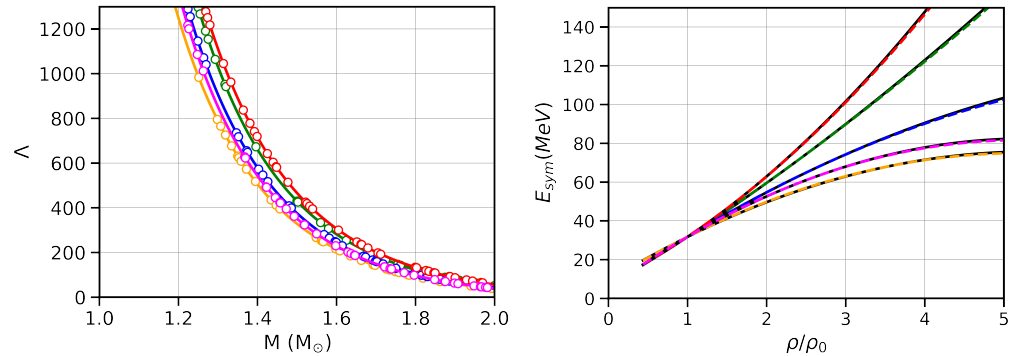
Figure 6. Example input $M(\Lambda)$ sequences (**left window**) and corresponding estimated $E_{sym}(\rho)$ (**right window**). The input samples consist of 50 randomly selected points, denoted by the "o" characters, from the genuine $M(\Lambda)$ curves, denoted by the solid lines, in the range of 1–2 $M_\odot$. All other figure features are the same as in Figure 5. See text for details.

6. Summary and Outlook

We have demonstrated, for the first time, the reconstruction of the nuclear symmetry energy directly from MMA observations of neutron stars using deep learning approaches. Specifically, we have shown that deep neural networks can extract $E_{sym}(\rho)$ accurately from either mass and radius $M - R$ or mass and tidal deformability $M - \Lambda$ astrophysical measurements of neutron stars. These results are a step towards realizing the goal of determining the EOS of dense nuclear matter, and they underline the importance and potential of the DL-based approach in the era of multi-messenger astrophysics, where an ever-increasing volume of MMA data is becoming rapidly available.

Future directions include considering the complete set of EOS parameters in Equations (2) and (3). Specifically, we will also take into account the effect of J_0 and J_{sym}, which are set to $J_0 = J_{sym} = 0$ in the current analysis. Despite the large current uncertainties of these higher-order parameters, their inclusion will allow us to model a much wider range of realistic EOSs, and thus enable a direct comparison of $E_{sym}(\rho)$ estimates, obtained with the DL techniques developed in this work, with realistic symmetry energies. Astrophysical observations of neutron stars inevitably carry error uncertainties, which lead to corresponding errors and uncertainties in the extracted symmetry energy, and EOS. For realistic applications of our approach, the effect of empirical errors and uncertainties needs to be considered and implemented consistently in the formalism. This can be achieved, for instance, by recasting the $E_{sym}(\rho)$ regression problem into a probabilistic framework. In subsequent works, we plan to implement Bayesian neural networks to perform the symmetry energy inference task. In this paradigm, instead of having deterministic values, the weights of these networks are characterized by probabilistic distributions by placing a prior over the network weights [171]. Finally, we also plan to investigate likelihood-free inference methods based on normalizing flows [172]. By applying a series of nonlinear transforms to a simple posterior shape (e.g., a multivariate Gaussian), the flow is able to reproduce complex posteriors without evaluating the likelihood directly. These techniques have already gained considerable interest in the research community, and, recently, a likelihood-free inference method based on normalizing flows was applied [173] to rapidly perform parameter estimation of eight BBH GW events in the first LIGO catalog, GWTC-1 [174]. Such rapid

processing will be particularly important for next-generation space telescopes and GW detectors, whose sensitivity goals will allow for the detection and observation of compact binary collisions, and neutron stars, throughout the history of the universe, exceeding a million events per year, with thousands of BNS detections/year alone. Conventional Bayesian inference approaches are not scalable to the study of thousands of BNS events per year, and modern normalizing flow models could certainly help to extract BNS parameters promptly and accurately.

Ultimately, as more events involving neutron stars are observed, these modern data-driven approaches will allow us to rapidly process the ever-increasing amount of neutron star observational data and determine precisely the nuclear symmetry energy and the EOS of dense nuclear matter.

Notes

[1] $\rho_0 = 0.16$ fm^{-1} is the saturation density of symmetric nuclear matter.

[2] At present, such a large number of simultaneous NS mass and radius (or M and Λ) measurements may look too optimistic. However, with the rapid advent of the next generation of telescopes and GW detectors, a much greater number of NS observations is expected in the near future.

References

1. The National Academies Press. *New Worlds, New Horizons in Astronomy and Astrophysics*; The National Academies Press: Washington, DC, USA, 2011. Available online: https://www.nap.edu/catalog/12951/new-worlds-new-horizons-in-astronomy-and-astrophysics (accessed on 28 September 2021).
2. The National Academies Press. *Nuclear Physics: Exploring the Heart of Matter*; Report of the Committee on the Assessment of and Outlook for Nuclear Physics; The National Academies Press: Washington, DC, USA, 2012. Available online: https://www.nap.edu/catalog/13438/nuclear-physics-exploring-the-heart-of-matter (accessed on 28 September 2021).
3. 2015 U.S. Long Range Plan for Nuclear Sciences. Available online: https://www.osti.gov/servlets/purl/1296778 (accessed on 28 September 2021).
4. Li, B.A.; Ramos, À.; Verde, G.; Vidaña, I. Topical Issue on Nuclear Symmetry Energy. *Eur. Phys. J. A* **2014**, *50*, 9. [CrossRef]
5. Li, B.-A.; Cai, B.-J.; Xie, W.-J.; Zhang, N.-B. Progress in Constraining Nuclear Symmetry Energy Using Neutron Star Observables Since GW170817. *Universe* **2021**, *7*, 182. [CrossRef]
6. Danielewicz, P.; Lacey, R.; Lynch, W.G. Determination of the equation of state of dense matter. *Science* **2002**, *298*, 1592–1596. [CrossRef] [PubMed]
7. Baran, V.; Colonna, M.; Greco, V.; Di Toro, M. Reaction dynamics with exotic nuclei. *Phys. Rep.* **2005**, *410*, 335–466. [CrossRef]
8. Steiner, A.W.; Prakash, M.; Lattimer, J.M.; Ellis, P.J. Isospin asymmetry in nuclei and neutron stars. *Phys. Rep.* **2005**, *411*, 325–375. [CrossRef]
9. Tsang, M.B.; Stone, J.R.; Camera, F.; Danielewicz, P.; Gandolfi, S.; Hebeler, K.; Horowitz, C.J.; Lee, J.; Lynch, W.G.; Kohley, Z.; et al. Constraints on the symmetry energy and neutron skins from experiments and theory. *Phys. Rev. C* **2012**, *86*, 015803. [CrossRef]
10. Baldo, M.; Burgio, G.F. The nuclear symmetry energy. *Prog. Part. Nucl. Phys.* **2016**, *91*, 203–258. [CrossRef]
11. Li, B.-A. Nuclear symmetry energy extracted from laboratory experiments. *Nucl. Phys. News* **2017**, *27*, 7–11. [CrossRef]
12. Li, B.-A.; Cai, B.J.; Chen, L.W.; Xu, J. Nucleon effective masses in neutron-rich matter. *Prog. Part. Nucl. Phys.* **2018**, *99*, 29–119. [CrossRef]
13. Burgio, G.F.; Vidaña, I. The Equation of State of Nuclear Matter: From Finite Nuclei to Neutron Stars. *Universe* **2020**, *6*, 119. [CrossRef]
14. Lattimer, J.M.; Prakash, M. Neutron star structure and the equation of state. *Astrophys. J.* **2001**, *550*, 426–442. [CrossRef]
15. Lattimer, J.M.; Prakash, M. The equation of state of hot, dense matter and neutron stars. *Phys. Rep.* **2016**, *621*, 127–164. [CrossRef]

16. Watts, A.L.; Andersson, N.; Chakrabarty, D.; Feroci, M.; Hebeler, K.; Israel, G.; Lamb, F.K.; Miller, M.C.; Morsink, S.; Özel, F.; et al. Colloquium: Measuring the neutron star equation of state using X-ray timing. *Rev. Mod. Phys.* **2016**, *88*, 021001. [CrossRef]
17. Özel, F.; Freire, P. Masses, radii, and the equation of state of neutron stars. *Annu. Rev. Astron. Astrophys.* **2016**, *88*, 401–440. [CrossRef]
18. Oertel, M.; Hempel, M.; Klähn, T.; Typel, S. Equations of state for supernovae and compact stars. *Rev. Mod. Phys.* **2017**, *89*, 015007. [CrossRef]
19. Baiotti, L. Gravitational waves from neutron star mergers and their relation to the nuclear equation of state. *Prog. Part. Nucl. Phys.* **2019**, *109*, 103714. [CrossRef]
20. Li, B.-A.; Krastev, P.G.; Wen, D.H.; Zhang, N.B. Towards understanding astrophysical effects of nuclear symmetry energy. *Eur. Phys. J. A* **2019**, *55*, 117. [CrossRef]
21. Weber, F.; Negreiros, R.; Roseneld, P.; Stejner, M. Pulsars as astrophysical laboratories for nuclear and particle physics. *Prog. Part. Nucl. Phys.* **2007**, *59*, 94–113. [CrossRef]
22. Alford, M.G.; Han, S.; Schwenzer, K. Signatures for quark matter from multi-messenger observations. *J. Phys. G Nucl. Part. Phys.* **2019**, *46*, 114001. [CrossRef]
23. Capano, C.D.; Tews, I.; Brown, S.M.; Margalit, B.; De, S.; Kumar, S.; Brown, D.A.; Krishnan, B.; Reddy, S. Stringent constraints on neutron-star radii from multimessenger observations and nuclear theory. *Nat. Astron.* **2020**, *4*, 625–632. [CrossRef]
24. Blaschke, D.; Ayriyan, A.; Alvarez-Castillo, D.E.; Grigorian, H. Was GW170817 a canonical neutron star merger? Bayesian analysis with a third family of compact stars. *Universe* **2020**, *6*, 81. [CrossRef]
25. Chatziioannou, K. Neutron-star tidal deformability and equation-of-state constraints. *Gen. Relativ. Gravit.* **2020**, *52*, 109. [CrossRef]
26. Annala, E.; Gorda, T.; Kurkela, A.; Vuorinen, A. Gravitational-Wave Constraints on the Neutron-Star-Matter Equation of State. *Phys. Rev. Lett.* **2018**, *120*, 172703. [CrossRef]
27. Kievsky, A.; Viviani, M.; Logoteta, D.; Bombaci, I.; Girlanda, L. Correlations imposed by the unitary limit between few-nucleon systems and compact stellar systems. *Phys. Rev. Lett.* **2018**, *121*, 072901. [CrossRef] [PubMed]
28. Landry, P.; Essick, R.; Chatziioannou, K. Nonparametric constraints on neutron star matter with existing and upcoming gravitational wave and pulsar observations. *Phys. Rev. D* **2020**, *101*, 123007. [CrossRef]
29. Dietrich, T.; Coughlin, M.W.; Pang, P.T.H.; Bulla, M.; Heinzel, J.; Issa, L.; Tews, I.; Antier, S. Multimessenger constraints on the neutron-star equation of state and the Hubble constant. *Science* **2020**, *370*, 1450–1453. [CrossRef] [PubMed]
30. Stone, J.R. Nuclear Physics and Astrophysics Constraints on the High Density Matter Equation of State. *Universe* **2021**, *7*, 257. [CrossRef]
31. Li, A.; Zhu, Z.Y.; Zhou, E.P.; Dong, J.M.; Hu, J.N.; Xia, C.J. Neutron star equation of state: Quark mean-field (QMF) modeling and applications. *J. High Energy Astrophys.* **2020**, *28*, 19–46. [CrossRef]
32. Burgio, G.F.; Vidaña I.; Schulze, H.-J.; Wei, J.-B. Neutron stars and the nuclear equation of state. *Prog. Part. Nucl. Phys.* **2021**, *120*, 103879. [CrossRef]
33. Burgio, G.F.; Schulze, H.J.; Vidaῆa, I.; Wei, J.B. A Modern View of the Equation of State in Nuclear and Neutron Star Matter. *Symmetry* **2021**, 13, 400. [CrossRef]
34. Krastev, P.G.; Li, B.-A. Imprints of the nuclear symmetry energy on the tidal deformability of neutron stars. *J. Phys. G* **2019**, *46*, 074001. [CrossRef]
35. Raithel, C.A.; Özel, F. Measurement of the nuclear symmetry energy parameters from gravitational wave events. *Astrophys. J.* **2019**, *885*, 121. [CrossRef]
36. Gendreau, K.; Arzoumanian, Z. Searching for a pulse. *Nat. Astron.* **2017**, *1*, 895. [CrossRef]
37. Aasi, J.; Abbott, B.P.; Abbott, R.; Abbott, T.; Abernathy, M.R.; Ackley, K.; Adams, C.; Adams, T.; Addesso, P.; Adhikari, R.X.; et al. Advanced LIGO. *Class. Quant. Grav.* **2015**, *32*, 074001. [CrossRef]
38. Acernese, F.A.; Agathos, M.; Agatsuma, K.; Aisa, D.; Allemandou, N.; Allocca, A.; Amarni, J.; Astone, P.; Balestri, G.; Ballardin, G.; et al. Advanced Virgo: a second-generation interferometric gravitational wave detector. *Class. Quant. Grav.* **2015**, *32*, 024001. [CrossRef]
39. KAGRA Collaboration. KAGRA: 2.5 generation interferometric gravitational wave detector. *Nat. Astron.* **2019**, *3*, 35–40. [CrossRef]
40. Bombaci, I.; Lombardo, U. Asymmetric nuclear matter equation of state. *Phys. Rev. C* **1991**, *44*, 1892. [CrossRef]
41. Hebeler, K.; Schwenk, A. Chiral three-nucleon forces and neutron matter. *Phys. Rev. C* **2010** *82*, 014314. [CrossRef]
42. Tews, I.; Krüger, T.; Hebeler, K.; Schwenk, A. Neutron matter at next-to-next-to-next-to-leading order in chiral effective field theory. *Phys. Rev. Lett.* **2013**, *110*, 032504. [CrossRef]
43. Holt, J.W.; Kaiser, N.; Weise, W. Nuclear chiral dynamics and thermodynamics. *Prog. Part. Nucl. Phys.* **2013**, *73*, 35. [CrossRef]
44. Hagen, G.; Papenbrock, T.; Ekström, A.; Wendt, K.A.; Baardsen, G.; Gandolfi, S.; Hjorth-Jensen, M.; Horowitz, C.J. Coupled-cluster calculations of nucleonic matter. *Phys. Rev. C* **2014**, *89*, 014319. [CrossRef]
45. Roggero, A.; Mukherjee, A.; Pederiva, F. Quantum Monte Carlo calculations of neutron matter with non-local chiral interactions. *Phys. Rev. Lett.* **2014**, *112*, 221103. [CrossRef] [PubMed]
46. Machleidt, R.; Entem, D.R. Chiral effective field theory and nuclear forces. *Phys. Rep.* **2011**, *503*, 1–75. [CrossRef]
47. Wlazłowski, G.; Holt, J.W.; Moroz, S.; Bulgac, A.; Roche, K.J. Auxiliary-Field Quantum Monte Carlo Simulations of Neutron Matter in Chiral Effective Field Theory. *Phys. Rev. Lett.* **2014**, *113*, 182503. [CrossRef] [PubMed]

48. Tews, I.; Carlson, J.; Gandolfi, S.; Reddy, S. Constraining the speed of sound inside neutron stars with chiral effective field theory interactions and observations. *Astrophys. J.* **2018**, *860*, 149. [CrossRef]

49. Drischler, C.; Furnstahl, R.J.; Melendez, J.A.; Phillips, D.R. How Well Do We Know the Neutron-Matter Equation of State at the Densities Inside Neutron Stars? A Bayesian Approach with Correlated Uncertainties. *Phys. Rev. Lett.* **2020**, *125*, 202702. [CrossRef]

50. Drischler, C.; Holt, J.W.; Wellenhofer, C. Chiral Effective Field Theory and the High-Density Nuclear Equation of State. *Ann. Rev. Nucl. Part. Sci.* **2021**, *71*, 1. [CrossRef]

51. Freedman, B.A.; McLerran,L.D. Fermions and Gauge Vector Mesons at Finite Temperature and Density. 1. Formal Techniques. *Phys. Rev. D* **1977**, *16*, 1130. [CrossRef]

52. Freedman, B.A.; McLerran, L.D. Fermions and Gauge Vector Mesons at Finite Temperature and Density. 3. The Ground State Energy of a Relativistic Quark Gas. *Phys. Rev. D* **1977**, *16*, 1169. [CrossRef]

53. Baluni, V. Nonabelian Gauge Theories of Fermi Systems: Chromotheory of Highly Condensed Matter. *Phys. Rev. D* **1978**, *17*, 2092. [CrossRef]

54. Kurkela, A.; Romatschke, P.; Vuorinen, A. Cold Quark Matter. *Phys. Rev. D* **2010**, 81, 105021. [CrossRef]

55. Fraga, E.S.; Kurkela, A.; Vuorinen, A. Interacting quark matter equation of state for compact stars. *Astrophys. J. Lett.* **2014**, *781*, L25. [CrossRef]

56. Gorda, T.; Kurkela, A.; Romatschke, P.; Säppi, M.; Vuorinen, A. Next-to-Next-to-Next-to-Leading Order Pressure of Cold Quark Matter: Leading Logarithm. *Phys. Rev. Lett.* **2018**, *121*, 202701. [CrossRef] [PubMed]

57. Ghiglieri, J.; Kurkela, A.; Strickland, M.; Vuorinen, A. Perturbative Thermal QCD: Formalism and Applications. *Phys. Rept.* **2020**, *880*, 1. [CrossRef]

58. Fujimoto, Y.; Fukushima, K.; Murase, K. Extensive Studies of the Neutron Star Equation of State from the Deep Learning Inference with the Observational Data Augmentation. *J. High Energ. Phys.* **2021**, *3*, 273. [CrossRef]

59. Aarts, G. Introductory lectures on lattice QCD at nonzero baryon number. *J. Phys. Conf. Ser.* **2016**, *706*, 022004. [CrossRef]

60. Li, B.-A.; Chen, L.-W.; Ko,C.M. Recent progress and new challenges in isospin physics with heavy-ion reactions. *Phys. Rep.* **2008**, *464*, 113–281. [CrossRef]

61. Li, B.-A.; Han, X. Constraining the neutron-proton effective mass splitting using empirical constraints on the density dependence of nuclear symmetry energy around normal density. *Phys. Lett. B* **2013**, *727*, 276–281. [CrossRef]

62. Horowitz, C.J.; Brown, E.F.; Kim, Y.; Lynch, W.G.; Michaels, R.; Ono, A.; Piekarewicz, J.; Tsang, M.B.; Wolter, H.H. A way forward in the study of the symmetry energy: experiment, theory, and observation. *J. Phys. G Nucl. Part. Phys.* **2014**, *41*, 093001. [CrossRef]

63. Lattimer, J.M.; Steiner, A.W. Constraints on the symmetry energy using the mass-radius relation of neutron stars. *Eur. Phys. J. A* **2014**, *50*, 40. [CrossRef]

64. Drago, A.; Lavagno, A.; Pagliara, G.; Pigato, D. Early appearance of Δ isobars in neutron stars. *Phys. Rev. C* **2014**, *90*, 065809. [CrossRef]

65. Cai, B.J.; Fattoyev, F.J.; Li, B.A.; Newton,W.G. Critical density and impact of $\Delta(1232)$ resonance formation in neutron stars. *Phys. Rev. C* **2015**, *92*, 015802. [CrossRef]

66. Zhu, Z.Y.; Li, A.; Hu, J.N.; Sagawa, H. $\Delta(1232)$ effects in density-dependent relativistic hartree-fock theory and neutron stars. *Phys. Rev. C* **2016**, *94*, 045803. [CrossRef]

67. Sahoo, H.S.; Mitra, G.; Mishra, R.; Panda, P.K.; Li, B.A. Neutron star matter with Δ isobars in a relativistic quark model. *Phys. Rev. C* **2018**, *98*, 045801. [CrossRef]

68. Li, J.J.; Sedrakian, A.; Weber, F. Competition between delta isobars and hyperons and properties of compact stars. *Phys. Lett. B* **2018**, *783*, 234–240. [CrossRef]

69. Li, J.J.; Sedrakian, A. Implications from GW170817 for Delta-isobar Admixed Hypernuclear Compact Stars. *Astrophys. J. Lett.* **2019**, *874*, L22. [CrossRef]

70. Ribes, P.; Ramos, A.; Tolos, L.; Gonzalez-Boquera, C.; Centelles, M. Interplay between Δ Particles and Hyperons in Neutron Stars. *Astrophys. J.* **2019**, *883*, 168. [CrossRef]

71. Raduta, A.R.; Oertel, M.; Sedrakian, A. Proto-neutron stars with heavy baryons and universal relations. *Mon. Not. R. Astron. Soc.* **2020**, *499*, 914–931. [CrossRef]

72. Raduta, A.R. Δ-admixed neutron stars: Spinodal instabilities and dUrca processes. *Phys. Lett. B* **2021**, *814*, 136070. [CrossRef]

73. Thapa, V.B.; Sinha, M.; Li, J.J.; Sedrakian, A. Massive Δ-resonance admixed hypernuclear stars with antikaon condensations. *Phys. Rev. D* **2021**, *103*, 063004. [CrossRef]

74. Sen, D. Variation of the Δ baryon mass and hybrid star properties in static and rotating conditions. *Phys. Rev. C* **2021**, *103*, 045804. [CrossRef]

75. Jiang, W.Z.; Li, B.-A.; Chen, L.W. Large-mass neutron stars with hyperonization. *Astrophys. J.* **2012**, *756*, 56. [CrossRef]

76. Providência, C.; Fortin, M.; Pais, H.; Rabhi, A. Hyperonic stars and the nuclear symmetry energy. *Front. Astron. Space Sci.* **2019**, *6*, 13. [CrossRef]

77. Vidaña, I. Hyperons: The strange ingredients of the nuclear equation of state. *Proc. R. Soc. Lond. A* **2018**, *474*, 20180145. [CrossRef] [PubMed]

78. Choi, S.; Miyatsu, T.; Cheoun, M.K.; Saito, K. Constraints on Nuclear Saturation Properties from Terrestrial Experiments and Astrophysical Observations of Neutron Stars. *Astrophys. J.* **2021**, *909*, 156. [CrossRef]

79. Fortin, M.; Raduta, A.R.; Avancini, S.; Providência, C. Thermal evolution of relativistic hyperonic compact stars with calibrated equations of state. *Phys. Rev. D* **2021**, *103*, 083004. [CrossRef]
80. Özel, F.; Baym, G.; Güver, T. Astrophysical Measurement of the Equation of State of Neutron Star Matter. *Phys. Rev. D* **2010**, *82*, 101301. [CrossRef]
81. Steiner, A.W.; Lattimer, J.M.; Brown, E.F. The Equation of State from Observed Masses and Radii of Neutron Stars. *Astrophys. J.* **2010**, *722*, 33. [CrossRef]
82. Steiner, A.W.; Lattimer, J.M.; Brown, E.F. The Neutron Star Mass-Radius Relation and the Equation of State of Dense Matter. *Astrophys. J. Lett.* **2013**, *765*, L5. [CrossRef]
83. Raithel, C.A.; Özel, F.; Psaltis, D. From Neutron Star Observables to the Equation of State. I. An Optimal Parametrization. *Astrophys. J.* **2016**, *831*, 44. [CrossRef]
84. Raithel, C.A.; Özel, F.; Psaltis, D. From Neutron Star Observables to the Equation of State. II. Bayesian Inference of Equation of State Pressures. *Astrophys. J.* **2017**, *844*, 156. [CrossRef]
85. Essick, R.; Tews, I.; Landry, P.; Reddy, S.; Holz, D.E. Direct Astrophysical Tests of Chiral Effective Field Theory at Supranuclear Densities. *Phys. Rev. C* **2020**, *102*, 055803. [CrossRef]
86. Demorest, P.B.; Pennucci, T.; Ransom, S.M.; Roberts, M.S.; Hessels, J.W. A two-solar-mass neutron star measured using Shapiro delay. *Nature* **2010**, *467*, 1081–1083. [CrossRef]
87. Antoniadis, J.; Freire, P.C.; Wex, N.; Tauris, T.M.; Lynch, R.S.; Van Kerkwijk, M.H.; Kramer, M.; Bassa, C.; Dhillon, V.S.; Driebe, T.; et al. A Massive Pulsar in a Compact Relativistic Binary. *Science* **2013**, *340*, 6131. [CrossRef] [PubMed]
88. Cromartie, H.T.; Fonseca, E.; Ransom, S.M.; Demorest, P.B.; Arzoumanian, Z.; Blumer, H.; Brook, P.R.; DeCesar, M.E.; Dolch, T.; Ellis, J.A.; et al. Relativistic Shapiro delay measurements of an extremely massive millisecond pulsar. *Nat. Astron.* **2020**, *4*, 72–76. [CrossRef]
89. Özel, F.; Psaltis, D.; Güver, T.; Baym, G.; Heinke, C.; Guillot. S. The Dense Matter Equation of State from Neutron Star Radius and Mass Measurements. *Astrophys. J.* **2016**, *820*, 28. [CrossRef]
90. Bogdanov, S.; Heinke, C.O.; Özel, F.; Güver, T. Neutron Star Mass-Radius Constraints of the Quiescent Low-mass X-ray Binaries X7 and X5 in the Globular Cluster 47 Tuc. *Astrophys. J.* **2016**, *831*, 184. [CrossRef]
91. Riley, T.E.; Watts, A.L.; Bogdanov, S.; Ray, P.S.; Ludlam, R.M.; Guillot, S.; Arzoumanian, Z.; Baker, C.L.; Bilous, A.V.; Chakrabarty, D.; et al. A NICER View of PSR J0030 + 0451: Millisecond Pulsar Parameter Estimation. *Astrophys. J. Lett.* **2019**, *887*, L21. [CrossRef]
92. Miller, M.C.; Lamb, F.K.; Dittmann, A.J.; Bogdanov, S.; Arzoumanian, Z.; Gendreau, K.C.; Guillot, S.; Harding, A.K.; Ho, W.C.; Lattimer, J.M.; et al. PSR J0030 + 0451 Mass and Radius from NICER Data and Implications for the Properties of Neutron Star Matter. *Astrophys. J. Lett.* **2019**, *887*, L24. [CrossRef]
93. Abbott, B.; Jawahar, S.; Lockerbie, N.; Tokmakov, K. (LIGO Scientific Collaboration and Virgo Collaboration). GW170817: Observation of Gravitational Waves from a Binary Neutron Star Inspiral. *Phys. Rev. Lett.* **2017**, *119*, 161101. [CrossRef]
94. Abbott, B.; Jawahar, S.; Lockerbie, N.; Tokmakov, K. (LIGO Scientific Collaboration and Virgo Collaboration). GW190425: Observation of a Compact Binary Coalescence with Total Mass 3.4 $M_\odot$. *Astrophys. J. Lett.* **2020**, *892*, L3. [CrossRef]
95. Abbott, R.; Abbott, T.D.; Abraham, S.; Acernese, F.; Ackley, K.; Adams, A.; Adams, C.; Adhikari, R.X.; Adya, V.B.; Affeldt, C.; et al. Observation of Gravitational Waves from Two Neutron Star–Black Hole Coalescences. *Astrophys. J. Lett.* **2021**, *915*, L5. [CrossRef]
96. Yagi, K.; Yunes, N. I-Love-Q. *Science* **2013**, *341*, 365. [CrossRef] [PubMed]
97. Yagi, K.; Yunes, N. I-Love-Q Relations in Neutron Stars and their Applications to Astrophysics, Gravitational Waves and Fundamental Physics. *Phys. Rev. D* **2013**, *88*, 023009. [CrossRef]
98. LeCun, Y.; Bengio, Y.; Hinton, G. Deep learning. *Nature* **2015**, *521*, 436–444. [CrossRef]
99. Goodfellow, I.; Bengio, Y.; Courville, A. *Deep Learning*; MIT Press: Cambridge, MA, USA, 2016. Available online: https://www.deeplearningbook.org (accessed on 28 September 2021).
100. He, K.; Zhang, X.; Ren, S.; Sun, J. Deep residual learning for image recognition. In Proceedings of the IEEE Conference on Computer Vision and Pattern Recognition (CVPR), Las Vegas, NV, USA, 27–30 June 2016; pp. 770–778.
101. Young, T.; Hazarika, D.; Poria, S.; Cambria, E. Recent trends in deep learning based natural language processing. *IEEE Comput. Intell. Mag.* **2018**, *13*, 55–75. [CrossRef]
102. Baker, N.; Alexander, F.; Bremer, T.; Hagberg, A.; Kevrekidis, Y.; Najm, H.; Parashar, M.; Patra, A.; Sethian, J.; Wild, S.; et al. *Workshop Report on Basic Research Needs for Scientific Machine Learning: Core Technologies for Artificial Intelligence*; USDOE Office of Science (SC): Washington, DC, USA, 2019. [CrossRef]
103. Pang, L.G.; Zhou, K.; Su, N.; Petersen, H.; Stöcker, H.; Wang, X.N. An equation-of-state-meter of quantum chromodynamics transition from deep learning. *Nat. Commun.* **2018**, *9*, 210. [CrossRef]
104. Mori, Y.; Kashiwa, K.; Ohnishi, A. Toward solving the sign problem with path optimization method. *Phys. Rev. D* **2017**, *96*, 111501. [CrossRef]
105. Porotti, R.; Tamascelli, D.; Restelli, M.; Prati, E. Coherent transport of quantum states by deep reinforcement learning. *Commun. Phys.* **2019**, *2*, 61. [CrossRef]
106. Rem, B.S.; KÃd'ming, N.; Tarnowski, M.; Asteria, L.; FlÃd'schner, N.; Becker, C.; Sengstock, K.; Weitenberg, C. Identifying quantum phase transitions using artificial neural networks on experimental data. *Nat. Phys.* **2019**, *15*, 917–920. [CrossRef]

107. Melko, R.G.; Carleo, G.; Carrasquilla, J.; Cirac, J.I. Restricted Boltzmann machines in quantum physics. *Nat. Phys.* **2019**, *15*, 887–892. [CrossRef]

108. Carleo, G.; Troyer, M. Solving the Quantum Many-Body Problem with Artificial Neural Networks. *Science* **2017**, *355*, 602. [CrossRef] [PubMed]

109. Shanahan, P.E.; Trewartha, D.; Detmold, W. Machine learning action parameters in lattice quantum chromodynamics. *Phys. Rev. D* **2018**, *97*, 094506. [CrossRef]

110. Liu, Z.; Tegmark, M. AI Poincarè: Machine Learning Conservation Laws from Trajectories. *Phys. Rev. Lett.* **2021**, *126*, 180604. [CrossRef]

111. Gomez, S.; Berger E.; Hosseinzadeh, G.; Blanchard, P.K.; Nicholl, M.; Villar, V.A. The Luminous and Double-peaked Type Ic Supernova 2019stc: Evidence for Multiple Energy Sources. *Astrophys. J.* **2021**, *913*, 143. [CrossRef]

112. Villar, V.A.; Hosseinzadeh, G.; Berger, E.; Ntampaka, M.; Jones, D.O.; Challis, P.; Chornock, R.; Drout, M.R.; Foley, R.J.; Kirshner, R.P.; et al. SuperRAENN: A Semisupervised Supernova Photometric Classification Pipeline Trained on Pan-STARRS1 Medium-Deep Survey Supernovae. *Astrophys. J.* **2020**, *905*, 94. [CrossRef]

113. Schwartz, M.D. Modern Machine Learning and Particle Physics. *Harv. Data Sci. Rev.* **2021**, *3*. [CrossRef]

114. Gabbard, H.; Williams, M.; Hayes, F.; Messenger, C. Matching Matched Filtering with Deep Networks for Gravitational-Wave Astronomy. *Phys. Rev. Lett.* **2018**, *120*, 141103. [CrossRef]

115. George, D.; Huerta, E.A. Deep neural networks to enable real-time multimessenger astrophysics. *Phys. Rev. D* **2018**, *97*, 044039. [CrossRef]

116. George, D.; Huerta, E.A. Deep Learning for real-time gravitational wave detection and parameter estimation: Results with Advanced LIGO data. *Phys. Lett. B* **2018**, *778*, 64. [CrossRef]

117. Gebhard, T.D.; Kilbertus, N.; Harry, I.; Schölkopf, B. Convolutional neural networks: A magic bullet for gravitational-wave detection? *Phys. Rev. D* **2019**, *100*, 063015. [CrossRef]

118. Wang, H.; Wu, S.; Cao, Z.; Liu, X.; Zhu, J.Y. Gravitational-wave signal recognition of LIGO data by deep learning. *Phys. Rev. D* **2020**, *101*, 104003. [CrossRef]

119. Lin, Y.C.; Wu, J.H.P. Detection of gravitational waves using Bayesian neural networks. *Phys. Rev. D* **2021**, *103*, 063034. [CrossRef]

120. Morales, M.D.; Antelis, J.M.; Moreno, C.; Nesterov, A.I. Deep Learning for Gravitational-Wave Data Analysis: A Resampling White-Box Approach. *Sensors* **2021**, *21*, 3174. [CrossRef] [PubMed]

121. Xia, H.; Shao, L.; Zhao, J.; Cao, Z. Improved deep learning techniques in gravitational-wave data analysis. *Phys. Rev. D* **2021**, *103*, 024040. [CrossRef]

122. Chua, A.J.K.; Vallisneri, M. Learning Bayesian Posteriors with Neural Networks for Gravitational-Wave Inference. *Phys. Rev. Lett.* **2020**, *124*, 041102. [CrossRef]

123. Green, S.R.; Gair, J. Complete parameter inference for GW150914 using deep learning. *Mach. Learn. Sci. Technol.* **2021**, *2*, 03LT01. [CrossRef]

124. Wei, W.; Huerta, E.A. Gravitational wave denoising of binary black hole mergers with deep learning. *Phys. Lett. B* **2020**, *800*, 135081. [CrossRef]

125. Krastev, P.G. Real-time detection of gravitational waves from binary neutron stars using artificial neural networks. *Phys. Lett. B* **2020**, *803*, 135330. [CrossRef]

126. Krastev, P.G.; Gill, K.; Villar, V.A.; Berger, E. Detection and parameter estimation of gravitational waves from binary neutron-star mergers in real LIGO data using deep learning. *Phys. Lett. B* **2021**, *815*, 136161. [CrossRef]

127. Lecun, Y.; Bottou, L.; Bengio, Y.; Haffner, P. Gradient-based learning applied to document recognition. *Proc. IEEE* **1998**, *86*, 2278–2324. [CrossRef]

128. Ferreira, M.; Providência, C. Unveiling the nuclear matter EoS from neutron star properties: a supervised machine learning approach. *J. Cos. Astropart. Phys.* **2021**, *7*, 11. [CrossRef]

129. Morawski, F.; Bejger, M. Neural network reconstruction of the dense matter equation of state derived from the parameters of neutron stars. *Astron. Astrophys.* **2020**, *642*, A78. [CrossRef]

130. Traversi, S.; Char, P. Structure of Quark Star: A Comparative Analysis of Bayesian Inference and Neural Network Based Modeling. *Astrophys. J.* **2020**, *905*, 9. [CrossRef]

131. Fujimoto, Y.; Fukushima, K.; Murase, K. Mapping neutron star data to the equation of state using the deep neural network. *Phys. Rev. D* **2020**, *101*, 054016. [CrossRef]

132. Stone, J.R.; Reinhard, P.G. The Skyrme Interaction in finite nuclei and nuclear matter. *Prog. Part. Nucl. Phys.* **2007**, *58*, 587–657. [CrossRef]

133. Vautherin, D.; Brink, D.M. Hartree-Fock Calculations with Skyrme's Interaction. I. Spherical Nuclei. *Phys. Rev. C* **1972**, *5*, 626–647. [CrossRef]

134. Quentin, P.; Flocard, H. Self-Consistent Calculations of Nuclear Properties with Phenomenological Effective Forces. *Annu. Rev. Nucl. Part. Sci.* **1978**, *28*, 523–594. [CrossRef]

135. Boguta, J.; Bodmer, A.R. Relativistic calculation of nuclear matter and the nuclear surface. *Nucl. Phys. A* **1977**, *292*, 413–428. [CrossRef]

136. Machleidt, R.; Holinde, K.; Elster, C. The Bonn Meson Exchange Model for the Nucleon Nucleon Interaction. *Phys. Rep.* **1987**, *149*, 1–89. [CrossRef]

137. Nagels, M.M.; Rijken, T.A.; de Swart, J.J. A Low-Energy Nucleon-Nucleon Potential from Regge Pole Theory. *Phys. Rev. D* **1978**, *17*, 768. [CrossRef]
138. Weinberg, S. Nuclear forces from chiral lagrangians. *Phys. Lett. B* **1990**, *251*, 288–292. [CrossRef]
139. Weinberg, S. Effective chiral lagrangians for nucleon-pion interactions and nuclear forces. *Nucl. Phys. B* **1991**, *363*, 3–18. [CrossRef]
140. Epelbaum, E.; Hammer, H.W.; Meißner, U.G. Modern theory of nuclear forces. *Rev. Mod. Phys.* **2009**, *81*, 1773–1825. [CrossRef]
141. Day, B.D. Elements of the Brueckner-Goldstone Theory of Nuclear Matter. *Rev. Mod. Phys.* **1967**, *39*, 719–744. [CrossRef]
142. Brockmann, R.; Machleidt, R. Relativistic nuclear structure. I. Nuclear matter. *Phys. Rev. C* **1990**, *42*, 1965–1980. [CrossRef]
143. Müther, H.; Sammarruca, F.; Ma, Z. Relativistic effects and three-nucleon forces in nuclear matter and nuclei. *Int. J. Mod. Phys. E* **2017**, *26*, 1730001. [CrossRef]
144. Akmal, A.; Pandharipande, V.R.; Ravenhall, D.G. Equation of state of nucleon matter and neutron star structure. *Phys. Rev. C* **1998**, *58*, 1804–1828. [CrossRef]
145. Wiringa, R.B.; Pieper, S.C.; Carlson, J.; Pandharipande, V.R. Quantum Monte Carlo calculations of A = 8 nuclei. *Phys. Rev. C* **2000**, *62*, 014001. [CrossRef]
146. Gandolfi, S.; Illarionov, A.Y.; Schmidt, K.E.; Pederiva, F.; Fantoni, S. Quantum Monte Carlo calculation of the equation of state of neutron matter. *Phys. Rev. C* **2009**, *79*, 054005. [CrossRef]
147. Kadanoff, L.; Baym, G. *Quantum Statistical Mechanics*; W.A. Benjamin Inc.: New York, NY, USA, 1962. [CrossRef]
148. Bogner, S.K.; Furnstahl, R.J.; Schwenk, A. From low-momentum interactions to nuclear structure. *Prog. Part. Nucl. Phys.* **2010**, *65*, 94–147. [CrossRef]
149. Vidaña, I.; Providência, C.; Polls, A.; Rios, A. Density dependence of the nuclear symmetry energy: A microscopic perspective. *Phys. Rev. C* **2009**, 80, 045806. [CrossRef]
150. Zhang, N.-B.; Li, B.-A.; Xu, J. Combined Constraints on the Equation of State of Dense Neutron-rich Matter from Terrestrial Nuclear Experiments and Observations of Neutron Stars. *Astrophys. J.* **2018**, *859*, 90. [CrossRef]
151. Cai, B.J.; Li, B.A. Auxiliary Function Approach for Determining Symmetry Energy at Supra-saturation Densities. *Phys. Rev. C* **2021**, *103*, 054611. [CrossRef]
152. Zhang, N.B.; Li, B.A. Extracting Nuclear Symmetry Energies at High Densities from Observations of Neutron Stars and Gravitational Waves. *Eur. Phys. J. A* **2019**, *55*, 39. [CrossRef]
153. Xie, W.J.; Li, B.A. Bayesian Inference of High-density Nuclear Symmetry Energy from Radii of Canonical Neutron Stars. *Astrophys. J.* **2019**, *883*, 174. [CrossRef]
154. Krastev, P.G.; Sammarruca, F. Neutron star properties and the equation of state of neutron-rich matter. *Phys. Rev. C* **2006**, *74*, 025808. [CrossRef]
155. Pethick, C.J.; Ravenhall, D.G.; Lorenz, C.P. The inner boundary of a neutron-star crust. *Nucl. Phys. A* **1995**, *584*, 675. [CrossRef]
156. Haensel, P. ; Pichon, B. Experimental nuclear masses and the ground state of cold dense matter. *Astron. Astrophys.* **1994**, *283*, 313–318.
157. Li, B.A.; Magno, M. Curvature-slope correlation of nuclear symmetry energy and its imprints on the crust-core transition, radius and tidal deformability of canonical neutron stars. *Phys. Rev. C* **2020**, *102*, 045807. [CrossRef]
158. Oppenheimer, J.R.; Volkoff, G.M. On Massive Neutron Cores. *Phys. Rev.* **1939**, *55*, 374. [CrossRef]
159. Hinderer, T.; Lackey, B.D.; Lang, R.N.; Read, J.S. Tidal deformability of neutron stars with realistic equations of state and their gravitational wave signatures in binary inspiral. *Phys. Rev. D* **2010**, *81*, 123016. [CrossRef]
160. Flanagan, E.E.; Hinderer, T. Constraining neutron-star tidal Love numbers with gravitational-wave detectors. *Phys. Rev. D* **2008**, *77*, 021502. [CrossRef]
161. Damour, T.; Nagar, A. Relativistic tidal properties of neutron stars. *Phys. Rev. D* **2009**, *80*, 084035. [CrossRef]
162. Hinderer, T. Tidal Love Numbers of Neutron Stars. *Astrophys. J.* **2008**, *677*, 1216. [CrossRef]
163. Postnikov, S.; Prakash, M.; Lattimer, J.M. Tidal Love numbers of neutron and self-bound quark stars. *Phys. Rev. D* **2010**, *82*, 024016. [CrossRef]
164. Emmert-Streib, F.; Yang, Z.; Feng, H.; Tripathi, S.; Dehmer, M. An Introductory Review of Deep Learning for Prediction Models With Big Data. *Front. Artif. Intell.* **2020**, *3*, 4. [CrossRef]
165. Neilsen, M.A. *Neural Networks and Deep Learning*; Determination Press. 2015. Available online: http://neuralnetworksanddeeplearning.com (accessed on 28 September 2021).
166. LeCun, Y.A.; Bottou, L.; Orr G.B.; Müller, K.R. Efficient BackProp. In *Neural Networks: Tricks of the Trade*; Lecture Notes in Computer Science; Springer: Berlin/Heidelberg, Germany, 2012; Volume 7700. [CrossRef]
167. Adhikari, D.; Albataineh, H.; Androic, D.; Aniol, K.; Armstrong, D.S.; Averett, T.; Gayoso, C.A.; Barcus, S.; Bellini, V.; Beminiwattha, R.S.; et al. Accurate Determination of the Neutron Skin Thickness of ^{208}Pb through Parity-Violation in Electron Scattering. *Phys. Rev. Lett.* **2021**, *126*, 172502.. [CrossRef] [PubMed]
168. Abadi, M.; Agarwal, A.; Barham, P.; Brevdo, E.; Chen, Z.; Citro, C.; Corrado, G.S.; Davis, A.; Dean, J.; Dean, J.; et al. TensorFlow: Large-Scale Machine Learning on Heterogeneous Distributed Systems. 2015. Available online: https://www.tensorflow.org (accessed on 28 September 2021).
169. Kingma, D.P.; Ba, J. Adam: A method for stochastic optimization. *arXiv* **2014**, arXiv:1412.6980.
170. Reddi, S.J.; Kale, S.; Kumar, S. On the convergence of Adam and beyond. *arXiv* **2019**, arXiv:1904.09237.

171. Perreault Levasseur, L.; Hezaveh, Y.D.; Wechsler, R.H. Uncertainties in Parameters Estimated with Neural Networks: Application to Strong Gravitational Lensing. *Astrophys. J. Lett.* **2017**, *850*, L7. [CrossRef]

172. Kobyzev, I.; Prince, S.J.D.; Brubaker, M.A. Normalizing Flows: An Introduction and Review of Current Methods. *IEEE Trans. Pattern Anal. Mach. Intell.* **2021**, *43*, 3964–3979. [CrossRef] [PubMed]

173. Dax, M.; Green, S.R.; Gair, J.; Macke, J.H.; Buonanno, A.; Schölkopf, B. Real-time gravitational-wave science with neural posterior estimation. *arXiv* **2021**, arXiv:2106.12594

174. Abbott, B.P.; Abbott, R.; Abbott, T.; Abraham, S.; Acernese, F.; Ackley, K.; Adams, C.; Adhikari, R.X.; Adya, V.B.; Affeldt, C.; et al. GWTC-1: A Gravitational-Wave Transient Catalog of Compact Binary Mergers Observed by LIGO and Virgo during the First and Second Observing Runs. *Phys. Rev. X* **2019**, *9*, 031040. [CrossRef]